

# Point Cloud Quality Assessment: Dataset Construction and Learning-based No-Reference Approach

YIPENG LIU, Cooperative Medianet Innovation Center, Shanghai Jiaotong University, China

QI YANG, Cooperative Medianet Innovation Center, Shanghai Jiaotong University, China

YILING XU, Cooperative Medianet Innovation Center, Shanghai Jiaotong University, China

LE YANG, Department of electrical and computer engineering, University of Canterbury, New Zealand

Full-reference (FR) point cloud quality assessment (PCQA) has achieved impressive progress in recent years. However, in many cases, obtaining the reference point cloud is difficult, so the no-reference (NR) methods have become a research hotspot. Few researches about NR objective quality metrics are conducted due to the lack of a large-scale subjective point cloud dataset. Besides, the distinctive property of the point cloud format makes it infeasible to apply blind image quality assessment (IQA) methods directly to predict the quality scores of point clouds. In this paper, we establish a large-scale PCQA dataset, which includes 104 reference point clouds and more than 24,000 distorted point clouds. In the established dataset, each reference point cloud is augmented with 33 types of impairments (e.g., Gaussian noise, contrast distortion, geometry noise, local loss, and compression loss) at 7 different distortion levels. Besides, inspired by the hierarchical perception system and considering the intrinsic attributes of point clouds, an end-to-end sparse convolutional neural network (CNN) is designed to accurately estimate the subjective quality. We conduct several experiments to evaluate the performance of the proposed network. The results demonstrate that the proposed network has reliable performance. The dataset presented in this work will be publicly accessible at <http://smt.sjtu.edu.cn>.

Key Words: 3D quality assessment, point cloud, large-scale dataset, sparse convolution, learning-based features.

## 1 INTRODUCTION

Recently, thanks to the increasing capability of 3D acquisition devices, point cloud has emerged as the most popular format for immersive media. A point cloud consists of a collection of points, each of which has geometric coordinates but may also contain a number of other attributes such as color, reflectance and surface normals. Point cloud has been used in many applications such as augmented reality (AR), autonomous driving, industrial robotics, documentation and facial landmarking [15, 41]. In practice, a variety of distortion could be involved and affect human perception. Developing PCQA can help to understand the distortion and carry out the quality optimization for point cloud. Generally, PCQA can be performed using subjective experiment and objective metrics. Because the subjective experiment is expensive and time-consuming, developing robust and effective objective quality assessment metrics is important. The well-known Moving Picture Experts Group (MPEG) has established an expert group to study point cloud quality metrics. However, different from 2D media, e.g., images and videos presented in the regular grid, the points of 3D point cloud are scattered in the spatial space. Therefore, it is infeasible to apply IQA methods [27] directly to measure the quality of point clouds, and how to extract effective features from scattered points needs further exploration.

---

Authors' addresses: Yipeng Liu, [liuyipeng@sjtu.edu.cn](mailto:liuyipeng@sjtu.edu.cn), Cooperative Medianet Innovation Center, Shanghai Jiaotong University, Dongchuan Road 800, Shanghai, China; Qi Yang, [yang\\_littleqi@sjtu.edu.cn](mailto:yang_littleqi@sjtu.edu.cn), Cooperative Medianet Innovation Center, Shanghai Jiaotong University, Dongchuan Road 800, Shanghai, China; Yiling Xu, [y1.xu@sjtu.edu.cn](mailto:y1.xu@sjtu.edu.cn), Cooperative Medianet Innovation Center, Shanghai Jiaotong University, Dongchuan Road 800, Shanghai, China; Le Yang, [le.yang@canterbury.ac.nz](mailto:le.yang@canterbury.ac.nz), Department of electrical and computer engineering, University of Canterbury, Christchurch 8041, Canterbury, New Zealand.

---

## 1.1 Motivation

Refer to the consensus in IQA, there are three different types of PCQA metrics, namely, full-reference (FR), reduced-reference (RR) and no-reference (NR) metrics. In FR-PCQA and RR-PCQA, whole and partial reference samples are required, while NR-PCQA only utilizes distorted samples. FR-PCQA was first studied and has shown impressive progress. Some FR-PCQA metrics have already been incorporated into the MPEG point cloud compression (PCC) technology standardisation, including the point-to-point (p2point) [14] and point-to-plane (p2plane) [29]. These metrics mainly leverage the point-wise spatial deformation between the reference and distorted samples, which neglects the fact that the human visual system (HVS) is more sensitive to structural distortions. Besides, color-dominated distortion also plays an important role in human perception, but these metrics do not take color-related features into consideration. Thus, many other metrics considering both geometry and color distortion have been proposed, such as PCQM [31] and GraphSIM [53].

However, in many cases, the reference point cloud is not even available. Therefore, developing NR metrics can further facilitate the application of point cloud in practice. To the best of our knowledge, no NR-PCQA method has been proposed yet due to the following reasons:

i) Lack of database. The first reason is the lack of point cloud datasets. The development of deep learning-based NR-PCQA methods relies on the richness of available data. The lack of a large-scale subjective point cloud dataset impedes the development of NR-PCQA methods. Unlike 2D images that are relatively easy to collect in a large volume, obtaining point cloud is far more costly. The existing PCQA datasets, e.g., SJTU-PCQA [54], only have a few hundred point cloud instances, which are not sufficient to derive learning-based NR metrics.

ii) Difficulty in data annotation. The second reason is that annotating point cloud samples for quality assessment is difficult. Different from the data annotation in other applications, the labels for PCQA are from subjective experiments. Generally, subjective experiments are expensive, time-consuming, and requiring strict control conditions. Considering that there are more than 24,000 samples in our newly developed database, and each sample needs at least sixteen subjects after outliers removal to collect Mean Opinion Score (MOS), it is very difficult to annotate the whole dataset via subjective experiment alone.

iii) Inefficient dense convolution. Traditional implementations of convolution operations are optimized for data on densely populated grids, and are unable to process disordered data efficiently such as point cloud. They normally have high memory usage and slow inference speed. Exploiting the data sparsity, [20] proposes sub-manifold sparse convolutional networks. [19] illustrates that sub-manifold sparse convolutions offer reliable performance in terms of sparsity invariance and reduced computing load in point cloud processing tasks. In this work, we shall propose an end-to-end sparse CNN that operates on the entire input point cloud to predict quality scores.

## 1.2 Our Approach

In this paper, we first establish a large-scale point cloud database which can support deep learning-based metric development; secondly, we annotate the database using the pseudo MOS proposed in [50]; finally, we propose a sparse CNN as the backbone to extract the hierarchical features for quality prediction.

In particular, we construct a large-scale PCQA dataset first. The distortion of point cloud is more complex than that of images. The photometric attribute of point cloud may be subject to similar distortions in 2D images, because point cloud is produced by the special light field camera, and the distortion induced during filming may appear in the produced point clouds, such as Gaussian noise. Besides, the data structure of point cloud leads to some unique distortions, such as geometric distortion. As a result, the point cloud distortion may lie in the geometry component, or attribute

component, or both of them. To better understand and study the point cloud distortion, we establish a PCQA dataset with the largest size available, which contains 104 reference point clouds with 33 types of distortions (such as Gaussian noise, contrast distortion, geometry noise, local loss and compression loss) at 7 different levels, leading to a total number of 24,024 distorted point clouds. Some reference point cloud sequence samples are chosen from [3–6, 33] which have already been applied in the PCC standard. Some other reference point cloud samples are crafted from the mesh format samples in [1, 7].

To annotate the newly established dataset, we conduct a large-scale subjective experiment first to obtain the subjective MOS. The subjective experiment is conducted with 1,320 distorted point cloud samples selected from the database covering all distortion types. Then, inspired by [50], we compute Spearman Rank Order Correlation Coefficient (SROCC) of FR-PCQA methods for each distortion type based on the subjective MOS and their predicted scores. The scores from the best FR-PCQA method for each distortion type are selected and normalized as pseudo MOS. Since the performance of some existing FR-PCQA algorithms has been shown to be consistent with the HVS under certain types of distortion, the pseudo MOS is applied to annotate the mass point cloud samples.

Finally, we employ a sparse tensor representation and attempt to develop a sparse CNN using Minkowski Engine [13]. We extract the hierarchical features from the designed network which is a stack of sparse convolutional layers and residual blocks. The feature vectors are generated from the globally pooled hierarchical features. Then, the feature vectors are fed into the regression module to predict the final quality scores.

We test the developed metric in this paper on the proposed LS-PCQA dataset and SJTU-PCQA dataset [54]. The experiment results demonstrate that the newly proposed sparse CNN exhibits reliable performance.

### 1.3 Contributions

The main contributions of this paper are as follows.

- We establish a large-scale PCQA database with 24,024 distorted point clouds derived from 104 original reference point clouds, each with 33 distorted versions at 7 different distortion levels. The dataset covers a wide range of impairments during production, coding, compression, transmission and presentation. To the best of our knowledge, it is the largest PCQA dataset at present.
- Based on the established database, we conduct a fairly large subjective experiment campaign to collect MOS. In the experiment, we recruit 224 candidates to score 1,320 distorted point clouds, and ensure at least 16 subjective scores are collected for each distorted point cloud according to the standard ITU-R BT.500 [8].
- We develop the first NR-PCQA metric via a sparse CNN with 1.2M parameters. The experiment results show that our proposed network has reliable performance.
- We further verify the reliability of generated pseudo MOS and the robustness of the proposed sparse CNN backbone. We also explore the sensitivity of convolutional features with different depths to various distortions and the effectiveness in improving the prediction accuracy of residual blocks in the proposed network. Besides, we design the additional PCQA backbones such as PointNet [35] and compare their performance in Section 5.

The rest of this paper is organized as follows. The related work is reviewed in Section 2. The proposed large-scale PCQA dataset is introduced in Section 3, and Section 4 presents the proposed NR-PCQA method with its performance analysis given in Section 5. Finally, the conclusion is drawn in Section 6.

## 2 RELATED WORK

This section reviews the development of point cloud quality assessment and the 3D feature extraction.

### 2.1 Quality Metrics

Most existing point cloud quality metrics evaluate distortion based on geometrical attributes only. Specifically, p2point [14] quantifies the distances between corresponding points to measure the degree of distortion. P2plane [29] improves over p2point by projecting the obtained p2point distances along the surface normal direction. The point-to-mesh (p2mesh) [42] reconstructs the surface and then measures the distance from a point to the surface, but the efficiency of p2mesh is heavily dependent on the accuracy of the surface reconstruction algorithm. Both p2point and p2plane have already been applied in the standardized MPEG PCC technology [32].

On the other hand, Alexiou *et al.* [9] propose to measure the geometrical distortion based on the angular difference of point normals. Javaheri *et al.* [24] propose a generalized Hausdorff distance by employing the  $K$ th lowest distance instead of the biggest distance to avoid that Hausdorff distance are over-sensitive to noise.

The aforementioned point-wise metrics ignore the fact that HVS is more sensitive to structural features. Besides, color information also plays an important role in PCQA. Considering the huge success of SSIM [48] in IQA, researchers start to consider spatial structural features as the quality index. Some of them take geometry and color into consideration simultaneously. Meynet *et al.* [30] propose to use the local curvature statistics to reflect the point cloud surface distortion, and further pool curvature and color lightness together via optimally-weighted linear combination [31]. Viola *et al.* [47] propose a quality assessment metric based on the color histogram. Alexiou *et al.* [10] incorporate four types of point cloud attributes, namely, geometry, normal vectors, curvature values and colors, into the form of SSIM [48]. Yang *et al.* [53] propose to extract point cloud color gradient using graph signal processing to estimate the point cloud quality.

Another idea for PCQA is to project the 3D point cloud into a number of 2D planes, and then the 2D IQA methods can be used, such as the ones from [9, 44, 54]. However, the selection of projection directions may significantly influence model performance. Besides, projection can cause information loss and limit the overall performance [53]. Therefore, the performance of these projection-based methods is not satisfactory under multiple types of distortions.

The point cloud quality metrics surveyed above are FR metrics, which means that the input of all these methods requires both the reference and distorted point clouds. However, in many cases, obtaining the original reference point clouds is not feasible, such as in transmission. NR metrics deserve serious treatment. Unfortunately, there are no NR metrics available.

### 2.2 3D Feature Description

The first step of learning-based PCQA is to extract the representative features. Early work in 3D applications uses the hand-crafted feature descriptors to discriminate the local geometry characteristic. Johnson *et al.* [25] propose to project adjacent points onto the tangent plane to describe the geometry characteristics. Tombari *et al.* [43] propose to use covariance matrices of point pairs. Salti *et al.* [38] propose to create a 3D histogram of normal vectors. Rusu *et al.* [36, 37] propose to build an oriented histogram using pairwise geometric properties. Guo *et al.* [21] provide a comprehensive review of such hand-crafted descriptors.

The powerful representation ability for learning-based methods has attracted more and more attention. The current research hotspots have been directed to learning-based 3D feature representation. Zeng *et al.* [56] propose to learn the 3D patch descriptors by leveraging a Siamese CNN.

Khoury *et al.* [26] propose to adopt the multi-layer perceptrons to map the 3D oriented histogram to a low-dimensional feature space. Deng *et al.* [16, 17] propose to adopt PointNet [35] for geometric feature description. Yew *et al.* [55] adopt PointNet to extract features in outdoor scene registration.

The representative feature needed for PCQA is quite different from other 3D applications such as 3D object classification, detection and segmentation. First, all the above work extracts a small patch or a set of key points, and then maps them to a lower-dimensional space. However, PCQA requires both local details and global understanding. The limitation of the receptive field will definitely reduce PCQA methods' performance. Moreover, the separate computation for overlapping 3D regions slows down feature extraction which affects the speed of PCQA. Lastly, PCQA aims at measuring the distortion level using both geometry and color attributes, while extracting 3D patches or key points itself introduces distortion which will affect the accuracy of PCQA metrics. Thus, designing a point-level quality metric is necessary for NR-PCQA.

Choy *et al.* [13] propose the Minkowski Engine, an extension of the sub-manifold sparse network [19] to higher dimensions. In this work, the proposed NR-PCQA method using the Minkowski Engine operates on the entire input point cloud without having to crop the data into patches. In this way, we can address the above-mentioned limitations by aggregating information from a large number of neighboring points.

### 3 LS-PCQA: LARGE-SCALE POINT CLOUD QUALITY ASSESSMENT DATASET

Designing a quality assessment metric based on deep learning needs a large amount of data to improve its robustness and generalization capability. For 2D images, several popular datasets are available, including LIVE [2], CSIQ [39], TID2008 [49], TID2013 [34], LIVE MD [51], LIVE Challenge [18], and Waterloo Exploration [28]. Among them, the Waterloo Exploration has the largest size and it contains 94,880 distorted pictures.

However, for 3D point clouds, only a few datasets have been built. They include PointXR [11], IRPC [23], and SJTU-PCQA [54], the largest size of which is only 420 samples. The limit in the amount of data can easily lead to overfitting of the learning-based metrics. Besides, the existing datasets have obvious weaknesses. On the one hand, the number of reference point clouds and that of the included distortion types are insufficient. On the other hand, the quality of some reference point clouds is not good enough, which can impact the results of subjective experiments. These drawbacks would greatly affect the development of NR-PCQA metrics.

The difficulty of establishing a large-scale PCQA database comes from two aspects. The first is the difficulty of obtaining enough original point clouds. To solve this problem, we collect mesh format data and convert them to point clouds to enlarge the availability of point clouds. The second lies in the annotation of dataset which requires well-conducted subjective experiment under strict control conditions. Since the subjective experiment is time-consuming and expensive, it is quite difficult to collect MOS for a large number of point clouds. To address this problem, the pseudo MOS is adopted here.

In this paper, 104 original reference point clouds are crafted from [1, 3–7, 33]. Each reference point cloud is distorted by 33 types of impairments under 7 distortion levels. In total, 24,024 distorted point clouds are generated. Table 1 compares the newly developed dataset and 3 other databases, which clearly shows that our dataset has a larger size and it covers more distortion types.

To annotate the established dataset, we split the whole dataset into three parts. Part I that was labeled via the subjective experiment is used to screen FR metrics for multiple distortion types to generate pseudo MOS for part II and part III. Part II is used to evaluate the accuracy of pseudo MOS. Part III is labeled using pseudo MOS only, which is utilized to increase dataset scale. Specifically, Part I contains 990 distorted samples randomly selected from the whole dataset and they are annotated through the subjective experiment. In sample selection, we confirm 30 distorted samples for each

Table 1. Comparison of existing PCQA datasets and the proposed dataset

Datasets	Reference samples	Distortions	Distorted samples
PointXR	5	-	-
IRPC	6	3	54
SJTU-PCQA	10	7	420
Proposed	104	33	24,024

of the 33 considered distortion types. The obtained MOS is used to conduct the selection of best FR-PCQA and nonlinear mapping function to compute the pseudo MOS (see Section 3.4). Part II contains 330 distorted samples, confirming 10 samples for each of the 33 distortion types. We use both subjective MOS and pseudo MOS to label these samples, and illustrate the accuracy of the pseudo MOS (see Section 3.5). Part III contains the remaining distorted samples, which is labeled by the pseudo MOS only. Considering the effectiveness of the pseudo MOS, Part III may be extended to arbitrary size to facilitate the construction of large-scale PCQA dataset.

### 3.1 Reference Point Clouds

The reference point clouds in the proposed database come from MPEG and JPEG point cloud datasets [3–6], as well as the 3D mesh database [1, 7, 33]. For cloud points from MPEG and JPEG datasets, a manual examination is conducted to obtain point clouds of high quality. For 3D mesh samples, we apply uniformly distributed random sampling to take sample points from the surface of mesh. Specifically, the surfaces of mesh are randomly sampled to obtain the Cartesian coordinate of the point clouds. For texture, the sampled points are colored by examining the texture material at the same positions. Fig. 1 illustrates the process of texture sampling.

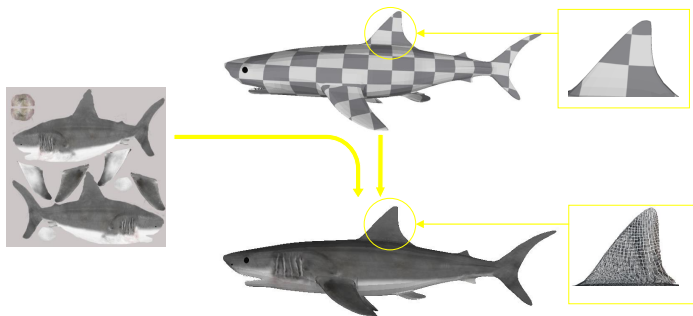


Fig. 1. Texture sampling for generating reference point clouds from mesh format data. We perform random sampling on the surfaces of the meshes to generate point clouds. Then the texture material is examined to color the selected points.

In total, 104 different point clouds, including 28 human models, 48 animal models and 28 inanimate objects, are chosen as the reference point cloud samples. All these reference point clouds are carefully screened to ensure their good quality, all of which score a MOS of 5 in the subjective experiment.

Table 2. Distortion types in the newly developed dataset, covering a wide range of impairments during production, coding, compression, transmission and presentation of point clouds.

No	Distortion Types	Typical Situation	Best FR-PCQA	No	Distortion Types	Typical Situation	Best FR-PCQA
#1	Color noise	Production	h.PSNRyuv	#18	Rayleigh noise	Transmission	PSNRyuv
#2	Color quantization with dither	Coding	PSNRyuv	#19	Saltpepper noise	Production, Transmission	MPED
#3	Contrast change	Production	h.PSNRyuv	#20	Change of color saturation	Presentation	PCQM
#4	Spatially correlated noise	Production	PSNRyuv	#21	Uniform noise (white noise)	Transmission	PSNRyuv
#5	Down sample	Coding	mseF,PSNR (p2point)	#22	Uniform geometry shifting	Transmission	MPED
#6	Gamma noise	Presentation	PSNRyuv	#23	VPCC-lossless G and lossy A	Compression	MPED
#7	Additive Gaussian noise	Production	PCQM	#24	VPCC-lossy G and lossless A	Compression	MPED
#8	Gaussian geometry shifting	Transmission	h.,PSNR (p2plane)	#25	VPCC-lossy G and lossy A	Compression	GraphSIM
#9	High frequency noise	Compression	PCQM	#26	AVS-limitlossy G and lossy A	Compression	mseF,PSNR (p2plane)
#10	Local loss	Transmission	GraphSIM	#27	AVS-lossless G and limitlossy A	Compression	h.PSNRyuv
#11	Local offset	Transmission	mseF,PSNR (p2point)	#28	AVS-lossless G and lossy A	Compression	h.PSNRyuv
#12	Local rotation	Transmission	h.,PSNR (p2point)	#29	GPCC-lossless G and lossy A	Compression	PCQM
#13	Luminance noise	Presentation	h.PSNRyuv	#30	GPCC-lossless G and nearlossless A	Compression	PCQM
#14	Mean shift (intensity shift)	Production	h.PSNRyuv	#31	GPCC-lossy G and lossy A	Compression	h.,PSNR (p2point)
#15	Multiplicative Gaussian noise	Production, Transmission	PCQM	#32	Octree Compression	Compression	h.,PSNR (p2point)
#16	Poisson noise	Production	PSNRyuv	#33	Poisson Reconstruction	Reconstruction	mseF,PSNR (p2point)
#17	Quantization noise	Coding	PCQM				

### 3.2 Distorted Point Clouds

Each reference point cloud is degraded by 33 types of impairments under 7 distortion levels, covering a wide range of impairments during production, coding, compression, transmission and presentation. A summary is given in Table 2. In total, 24,024 distorted point clouds are generated.

### 3.3 Obtaining the subjective MOS

To select the best FR-PCQA metrics for each distortion type and verify the accuracy of pseudo MOS, we annotate Part I and Part II of the dataset using the subjective experiment. The double stimulus method is adopted for subjective rating. We strictly follow the steps proposed by ITU-R Recommendation BT. 500 [8]. The configuration of subjective experiment is shown in Table 3.

Table 3. Setup of subjective experiment

Total number of point clouds	1,320
Number of scores for each point cloud	16
Viewing time for each participant	0.5h
Number of point clouds viewed by each participant	100
Number of participants	224

In the experiment, the participants sit in a controlled environment. Specifically, the zoom rate is set as 1:1. The presentation device used in subjective experiments is Dell SE2216H with a 21.5-inch monitor having a resolution of 1920×1080 pixels. The sitting posture of the participants is adjusted to ensure their eyes are at the same height as the center of the screen. The viewing distance is

about three times the height of the rendered point cloud ( $\approx 0.75$  meters). The subjective experiment is conducted indoors, under a normal lighting condition.

In the subjective experiment, only rotation operation is allowed to emulate the free-view navigation. This is because the distance to the 3D object will influence the subjective perception significantly. Even for a point cloud with good quality, it will show some holes if we zoom in too much. For participants who are lack of enough prior knowledge of point clouds, this phenomenon will bias their judgment. Therefore, we use the function ‘zoom rate’ provided by CloudCompare to fix the viewing distance, which maintains the consistency of viewing experience across participants.

Each pair of point clouds takes about 20 seconds for each participant to examine, leaving the next 5 seconds for the rating before the next pair is presented. The given scores are in the range of [1, 5] which corresponds to five quality levels shown in Table 4. At least 16 subjective scores are collected for each distorted point cloud.

Table 4. MOS score

5	Almost no distortion is perceived
4	Distortion can be perceived but don't hinder the viewing
3	Distortion slightly obstructs the viewing
2	Distortion definitely obstructs the viewing
1	Distortion seriously hinders the viewing

The screening method described in BT. 500 [8] is applied to remove the outliers whose scores are inconsistent with others. As a result, 14 participants are identified as outliers and removed. The scores from remaining 210 participants are kept for the following analysis.

We present the MOS distribution in Fig. 2 and Fig. 3 to demonstrate the validity of subjective data. Fig. 2 shows the MOS distribution for distorted point clouds. It can be seen from Fig. 2 that the subjective scores are spread across various MOS levels. Fig. 3 shows the average MOS for different distortion levels under each distortion type, which demonstrates the consistency between the average MOS and distortion levels.

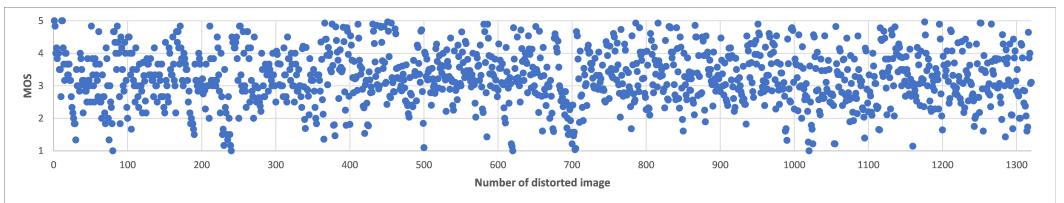


Fig. 2. MOS for point clouds in the proposed LS-PCQA .

### 3.4 Generation of Pseudo MOS

**3.4.1 Selection of Best FR-PCQA for Each Distortion Type.** Inspired by the pseudo MOS for images [50], we use FR metrics to annotate the samples for the proposed database. In order to select the best FR metric under different distortion types, 8 state-of-the-art quality metrics are examined, including p2point [14, 32], p2plane [29, 32], Hausdorff.p2point [14, 32], Hausdorff.p2plane [29, 32], PSNRyuv [32], Hausdorff.PSNRyuv [32], PCQM [31], GraphSIM [53] and MPED [52]. Table 5 lists the SROCC of these quality metrics on each distortion type based on the subjective MOS of Part I, and the best results are highlighted in bold.

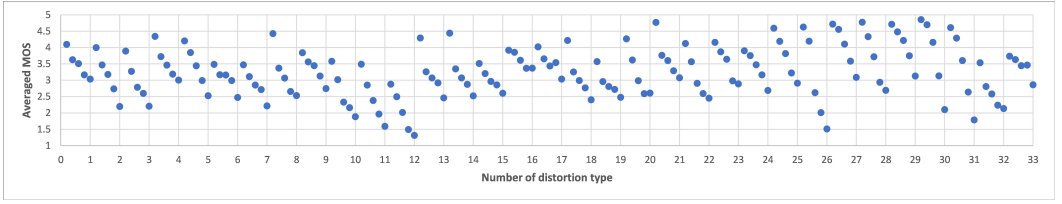


Fig. 3. MOS averaged for different distortion levels under each distortion type. The distortion types are indexed in the same order as in Table 5.

Table 5. SROCC of FR-PCQAs for each distortion type.

No	Distortion Type	mseF,PSNR (p2point)	mseF,PSNR (p2plane)	h.,PSNR (p2point)	h.,PSNR (p2plane)	PSNRyuv	h.PSNRyuv	PCQM	GraphSIM	MPED
#1	ColorNoise	-	-	-	-	0.833986	<b>0.847526</b>	0.815255	0.686812	0.786489
#2	ColorQuantization Dither	-	-	-	-	<b>0.825952</b>	0.749026	0.769419	0.516804	0.638994
#3	ContrastDistortion	-	-	-	-	0.689448	<b>0.765722</b>	0.743989	0.678540	0.374221
#4	CorrelatedGaussian Noise	-	-	-	-	<b>0.939239</b>	0.915869	0.850657	0.589139	0.665702
#5	DownSample	<b>0.881299</b>	0.626544	0.841531	0.811972	0.014907	-0.016913	0.524864	0.842585	0.857492
#6	GammaNoise	-	-	-	-	<b>0.749555</b>	0.682405	0.707703	0.588379	0.733081
#7	GaussianNoise	-	-	-	-	0.919226	0.903183	<b>0.950823</b>	0.769025	0.342164
#8	GaussianShifting	0.741433	0.718959	0.829773	<b>0.834223</b>	0.755229	0.235674	0.816199	0.742768	0.598353
#9	HighFrequencyNoise	-	-	-	-	0.836319	0.803160	<b>0.915100</b>	0.762880	0.800712
#10	LocalLoss	0.536227	0.497941	0.036992	0.302997	0.689371	0.364701	0.770840	<b>0.871007</b>	0.565895
#11	LocalOffset	<b>0.937340</b>	0.934669	0.770490	0.770738	0.667112	0.019499	0.851642	0.906177	0.897719
#12	LocalRotation	0.819668	0.712649	<b>0.831126</b>	0.734499	0.327066	0.004901	0.657248	0.723854	0.742183
#13	LumaNoise	-	-	-	-	0.772672	<b>0.855360</b>	0.748414	0.817848	0.715923
#14	MeanShift	-	-	-	-	0.422259	<b>0.818676</b>	0.614734	0.706210	0.727131
#15	Multiplicative GaussianNoise	-	-	-	-	0.751224	0.563910	<b>0.754339</b>	0.648420	0.687361
#16	PoissonNoise	-	-	-	-	<b>0.682406</b>	0.680179	0.662584	0.421827	0.366815
#17	QuantizationNoise	-	-	-	-	0.780537	0.398172	<b>0.848013</b>	0.617971	0.709498
#18	RayleighNoise	-	-	-	-	<b>0.893835</b>	0.804362	0.837748	0.706877	0.732918
#19	SaltpepperNoise	-	-	-	-	0.394971	0.044449	0.637517	0.560080	<b>0.698709</b>
#20	SaturationDistortion	-	-	-	-	0.739290	0.791143	<b>0.850562</b>	0.703016	0.597530
#21	UniformNoise	-	-	-	-	<b>0.898209</b>	0.871511	0.685727	0.645456	0.714651
#22	UniformShifting	0.851675	0.851675	0.857461	0.849672	0.796929	0.404542	0.638923	0.869701	<b>0.890175</b>
#23	VPCC_lossless-geom-lossy-attrs	-0.234650	-0.162450	0.139888	-0.020306	0.108403	-0.360601	0.193879	0.356372	<b>0.635726</b>
#24	VPCC_lossy-geom-lossless-attrs	0.414108	0.414998	0.323097	0.473743	0.284379	0.123275	0.520249	0.485759	<b>0.811081</b>
#25	VPCC_lossy-geom-lossy-attrs	0.753449	0.753004	0.640854	0.632844	0.372052	-0.005563	0.795505	<b>0.808189</b>	0.731420
#26	AVS_limitlossyG-lossyA	0.934698	<b>0.945823</b>	0.939598	0.929384	0.882412	0.337524	-	0.743907	0.937590
#27	AVS_losslessG-limitlossyA	-	-	-	-	0.837784	<b>0.885227</b>	-	0.877170	0.815754
#28	AVS_losslessG-lossyA	-	-	-	-	0.916352	<b>0.936927</b>	-	0.795773	0.870078
#29	GPCC_lossless-geom-lossy-attrs	-	-	-	-	0.567931	0.734839	<b>0.862134</b>	0.664515	0.517192
#30	GPCC_lossless-geom-nearlossless-attrs	-	-	-	-	0.878282	0.932864	<b>0.937695</b>	0.899421	0.817312
#31	GPCC_lossy-geom-lossy-attrs	0.955370	0.925543	<b>0.960451</b>	0.946853	0.730774	0.197663	0.844964	0.867446	0.903283
#32	octree	0.779039	0.788162	<b>0.819856</b>	0.752114	0.523810	0.108589	0.676235	0.757454	0.710948
#33	Possion Reconstruction	<b>0.847028</b>	0.835449	0.812514	0.811401	0.213093	-0.137609	0.720553	0.647518	0.719662

Table 5 indicates that adopting a single quality assessment method to label the whole dataset is insufficient and inaccurate. Each quality assessment method has its own limitations. Although

some quality metrics achieve the best results for certain distortion types, they may have poor performance or even cannot respond to some other distortion types. For example, p2point has achieved the best performance for some geometry distortions, but it is insensitive to photometric attribute distortion. PCQM achieves a SROCC of 0.950823 for Gaussian noise distortion, but for VPCC lossless-geom-lossy-attrs distortion, its SROCC is only 0.193879. Thus, we keep the best result among these quality metrics for each distortion type to annotate the distorted point clouds.

**3.4.2 Nonlinear Mapping.** The range of each quality metric is different from each other. To label the distorted point clouds, normalization is performed to re-scale the results to cast them under the same range. The commonly used nonlinear regression functions include four-parameter logistic regression (Logistic-4) [45], five-parameter logistic regression (Logistic-5) [40], and four-parameter polynomial regression (Cubic-4) [22, 46].

Logistic-4 applies

$$Q = \frac{\beta_1 - \beta_2}{1 + e^{-\frac{Q_s - \beta_3}{|\beta_4|}}} + \beta_2 \quad (1)$$

where  $Q$  is the normalized score,  $Q_s$  is the quality score predicted by the best quality assessment metric and  $\beta_1, \beta_2, \beta_3, \beta_4$  are the fitting parameters.

Logistic-5 achieves normalization via

$$Q = \beta_1 \left( \frac{1}{2} - \frac{1}{1 + e^{\beta_2(Q_s - \beta_3)}} \right) + \beta_4 Q_s + \beta_5 \quad (2)$$

where  $\beta_1, \beta_2, \beta_3, \beta_4, \beta_5$  are the parameters to be determined.

Cubic-4 uses the following for normalization

$$Q = aQ_s^3 + bQ_s^2 + cQ_s + d \quad (3)$$

where  $a, b, c, d$  are the model parameters.

In order to select the most appropriate mapping function, a validation experiment is conducted using Part I of the newly established dataset. The three nonlinear regression functions in consideration are adopted for MOS score normalization to project the best-predicting quality metric for each distortion type to the range of subjective MOS (i.e., 1-5). In this process, the monotonicity of the scores from different FR metrics may be different due to the use of different nonlinear functions, as shown in Fig. 4. Then, SROCCs based on the normalized scores and subjective MOS are computed for each nonlinear regression function. The results are listed in Table 6, with the best results highlighted in bold.

Table 6. Comparison of regression results for three nonlinear regression functions in consideration.

	Logistic-4	Logistic-5	Cubic-4
SROCC	0.857299	<b>0.902697</b>	0.895769
PLCC	0.862648	<b>0.910713</b>	0.904457

It can be seen from Table 6 that Logistic-5 offers the best results. Thus, Logistic-5 is adopted as the nonlinear normalization function for MOS score conversion in this work. The normalized pseudo MOS are used as the labels for the proposed large-scale dataset.

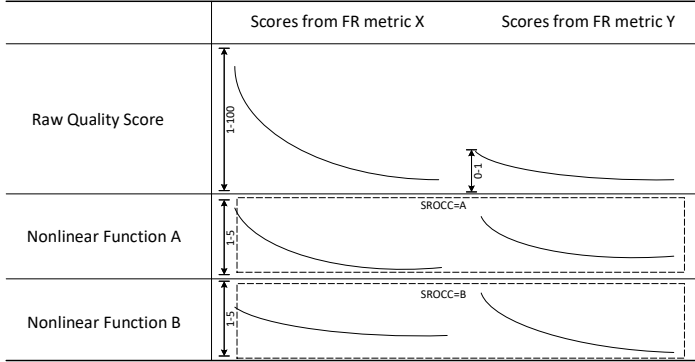


Fig. 4. Impact of piecewise mapping on SROCC. The nonlinear mapping will not change the SROCC of the scores from the same FR metric, but the overall SROCC may be changed after the normalization.

### 3.5 Accuracy Analysis of Pseudo MOS

We verify the reliability of the pseudo MOS scores via conducting the validation experiment using samples from Part I and Part II of the partitioned dataset. Note that Part II of the dataset is not used in the selection of full-reference metrics to generate the pseudo MOS. The SROCCs based on the subjective MOS and generated pseudo MOS in Part I and Part II are computed and listed in Table 7.

Table 7. Comparison between the pseudo and subjective MOS over Part I and Part II of the dataset.

	Part I	Part II
SROCC	0.902697	0.878517
PLCC	0.910713	0.871917

We can see from Table 7 that the SROCCs between the subjective and pseudo MOS of Part I and Part II are 0.902697 and 0.878517 respectively, which verifies the accuracy of the computed pseudo MOS and validity of the proposed annotation method.

Statistical analysis of annotation errors for samples in Part I and Part II is conducted. The annotation error represents  $MOS - pseudoMOS$ . The histograms of annotation errors for Part I and Part II are shown in Fig 5. The mean, standard deviation and 95% quantile of annotation errors for Part I and Part II are summarized in Table 8. Fig. 5 shows that most annotation errors have small magnitudes, even for the samples in Part II that are not used in the selection of FR metrics. These results corroborate that the pseudo MOS scores can be considered accurate approximation of the costly subjective MOS.

Table 8. Mean, standard deviation and 95% quantile of the annotation errors.

	Part I	Part II
Mean	0.0653	-0.0435
Standard deviation	0.4057	0.4804
95% quantile	0.7209	0.6752

To gain more insights, we present the annotation error statistics as a function of the distortion levels in Table 9. We can see that the pseudo MOS exhibits improved accuracy under more severe

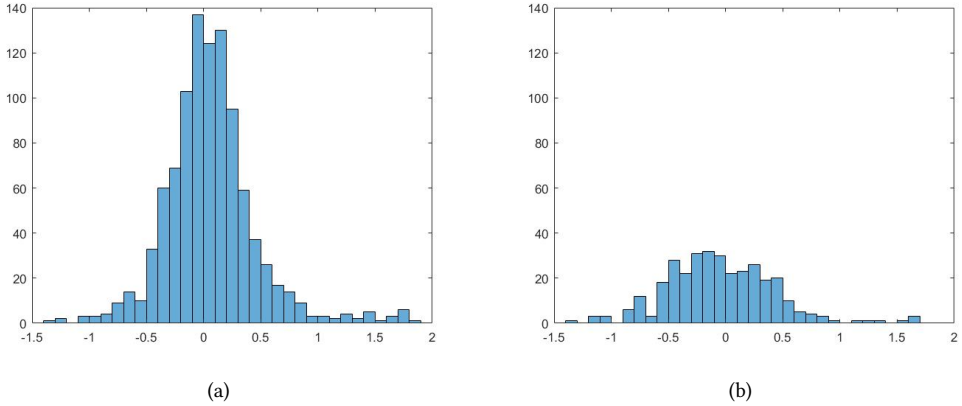


Fig. 5. Histograms of annotation error. (a) for Part I; (b) for Part II.

distortions. This is in fact expected, as the HVS would be more sensitive to obvious distortions, which can be better captured by FR metrics.

Table 9. Mean, standard deviation and 95% quantile with different distortion levels.

Distortion level	Slight	Low	Medium	High	Serious
Mean	0.1433	0.102	0.0627	0.0158	0.0029
Standard deviation	0.4315	0.4322	0.4070	0.3522	0.3870
95% quantile	1.0058	0.8068	0.6877	0.5841	0.6533

Finally, we list some examples of distorted point clouds with subjective MOS and pseudo MOS in the established dataset in Fig 6. It can be observed that the subjective MOS and pseudo MOS are quite close to each other in these examples.



Fig. 6. Exemplary quality point clouds with subjective MOS and pseudo MOS in the established dataset.

## 4 RESSCNN: AN SPARSE CNN FOR PCQA

An end-to-end learning-based NR-PCQA framework is proposed in this section. The source code for the proposed ResSCNN can be found at <https://github.com/lyp22/ResSCNN>.

### 4.1 Network Architecture

As shown in Fig. 7, the proposed framework for NR-PCQA consists of three modules: a feature extraction module  $W^f$ , a global pooling module  $\Phi$  and a regression module  $W^r$ . The feature extraction module uses a stack of sparse convolutional layers and residual blocks to extract hierarchical features. The global pooling module applies the global pooling operation to generate feature vectors from the input extracted hierarchical features. The regression module uses a concatenation of fully connected layers to map the feature vectors to the predicted quality scores.

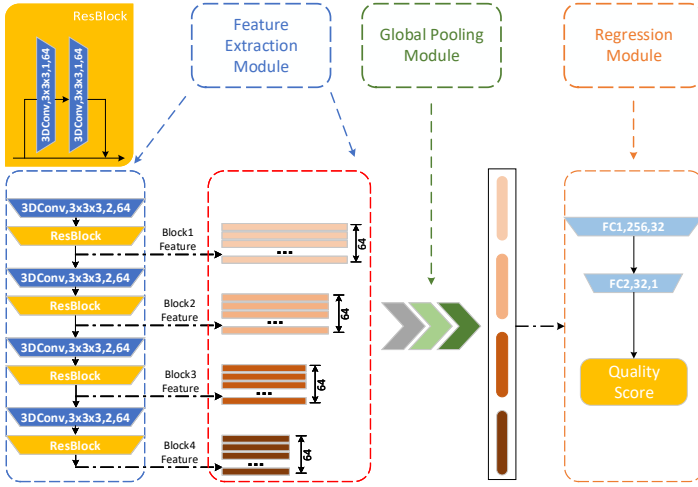


Fig. 7. Proposed framework architecture. The hierarchical features extracted from the sparse CNN are concatenated to be fed into the regressor to obtain the predicted quality score.

### 4.2 Feature Extraction Module

The feature extraction module is composed of four blocks. Each block consists of three sparse convolutional layers, in which the second and third sparse layers are connected to the residual pattern. The input of feature extraction module is the sparse tensor of the point cloud with the arbitrary number of points. The feature tensor  $F$  in the input sparse tensor has 3 feature dimensionalities referring to the color attributes of point cloud. Each sparse convolutional layer in Fig. 7 is characterized by the kernel size, stride and dimensionality, and is followed by batch normalization before being fed to the nonlinearity activation function (ReLU).

In the proposed network, the point cloud is represented by sparse tensors instead of traditional dense tensors. Mathematically, a sparse tensor for point cloud  $P \in R^{N \times 6}$  is represented as a set of coordinates  $C$  and associated features  $F$ :

$$C = \begin{bmatrix} x_1 & y_1 & z_1 & b_1 \\ \vdots & \vdots & \vdots & \vdots \\ x_N & y_N & z_N & b_N \end{bmatrix}, F = \begin{bmatrix} f_1^T \\ \vdots \\ f_N^T \end{bmatrix} \quad (4)$$

where  $x_i, y_i, z_i \in Z$  are the 3D coordinates of point  $i$ ,  $b_i$  is the batch index to distinguish points occupying the same coordinates but belonging to different batches, and  $f_i \in N^{3 \times 1}$ ,  $f_i \in [0, 255]$  is the R, G, B attributes associated with the  $i$ -th point.

The *3DConv* in the proposed network refers to the generalized sparse convolution in the Minkowski Engine [13], which is denoted as

$$x_u^{out} = \sum_{i \in N^D(u, C^{in})} W_i x_{u+i}^{in} \text{ for } u \in C^{out} \quad (5)$$

where  $N^D$  is a set of offsets that define the shape of a kernel and  $N^D(u, C^{in}) = \{i | u+i \in C^{in}, i \in N^D\}$  as the set of offsets from the current center,  $u \in C^{in}$ , that denotes the location.  $C^{in}$  and  $C^{out}$  are predefined input and output coordinates of sparse tensors.  $W_i$  denotes the kernel value at offset  $i$ .

The sparse convolution, instead of the dense convolution, is adopted to extract the features of the input point cloud. The dense convolution will result in a massive increase in the number of points of point cloud after convolution. This is shown in Fig. 8 where a point cloud is input into one layer of sparse convolution and dense convolution respectively. The sparse convolution and dense convolution are both characterized by a kernel size of  $3 \times 3 \times 3$ , stride of  $1 \times 1 \times 1$ , and dimensionality of 1 channel. We can see clearly that the dense convolution reduces the sparsity of point cloud.

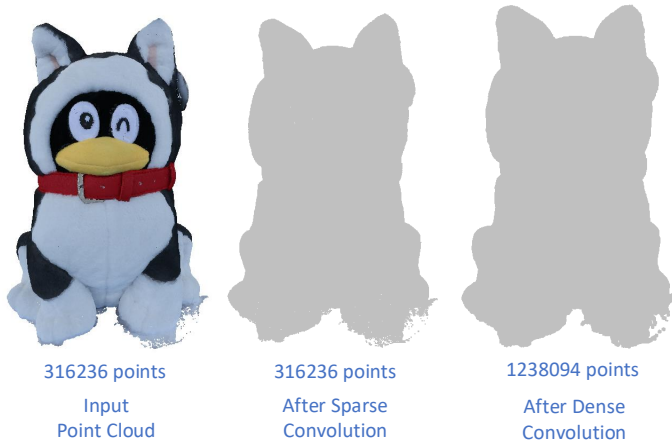


Fig. 8. Comparison between the sparse convolution and dense convolution. A point cloud is input into one layer of sparse convolution and dense convolution respectively.

### 4.3 Global Pooling Module

The branches of the global pooling module come from the output of each block in the feature extraction module. To deal with the output of each block with different shapes, the features extracted from the sparse CNN are globally pooled into  $64 \times 1$  feature vectors. Then the obtained four  $64 \times 1$  feature vectors are concatenated to form the  $256 \times 1$  representative hierarchical feature vector.

### 4.4 Regression Module

The regression module is composed of two fully connected layers, FC-1 and FC-2, to map the hierarchical feature vector to the predicted quality score. The input channel of FC-1 is 256, which

is the same as the length of the hierarchical features. The output channel of FC-1 and the input feature of FC-2 are 32. The output of the regression module is a predicted quality score of 1 channel.

In global pooling module, global pooling is applied to obtain the feature vector of different depths from the sparse CNN, which can be denoted as

$$S_i = \Phi_i(X; W^f), i = 1, \dots, K \quad (6)$$

where  $S_i \in R^{64 \times 1}$  represents the obtained feature vector from different depths of feature extraction module,  $W^f$  denotes the parameters of the feature extraction module, and the operation  $\Phi_i$  denotes the global pooling applied to the original deep convolutional features. The hierarchical features obtained from the global pooling module are

$$S = S_1 \oplus S_2 \oplus S_3 \oplus S_4 \quad (7)$$

where  $\oplus$  denotes the concatenation operation. The final predicted quality scores are found via

$$Q = F(S; W^r) \quad (8)$$

where  $Q$  is the predicted quality score,  $F$  represents the fully connected layers, and  $W^r$  denotes the parameters of the regression module.

#### 4.5 Loss Function

$L_1$  loss  $L_1(x) = |x|$  will fluctuate around the stable value, and converging to achieve higher accuracy is difficult. The gradient of  $L_2$  loss  $L_2(x) = x^2$  to the predicted value at the beginning of training is large and the training is unstable. Since smooth  $L_1$  loss combines the advantages of  $L_1$  loss and  $L_2$  loss, and avoids their disadvantages, smooth  $L_1$  loss is adopted to improve the robustness of the network:

$$SmoothL_1(x) = \begin{cases} 0.5x^2, & \text{if } |x| < 1 \\ |x| - 0.5, & \text{otherwise} \end{cases} \quad (9)$$

where  $x = q - \bar{q}$ ,  $q$  is the predicted quality score and  $\bar{q}$  is the ground truth. The gradient of loss function to  $x$  is formulated as

$$\frac{\partial smoothL_1(x)}{\partial x} = \begin{cases} x, & \text{if } |x| < 1 \\ \pm 1, & \text{otherwise} \end{cases} \quad (10)$$

where we can see that when  $x = q - \bar{q}$  is small, the gradient to  $x$  becomes smaller. When  $x$  is large, the upper limit of the gradient to  $x$  is 1, to ensure that derivatives are continuous for all degrees.

The training of network for point clouds consumes much more time than that of training using 2D images. To accelerate the speed of training, Stochastic Gradient Descent (SGD) is adopted with a learning rate  $1e-3$  with an exponential learning rate schedule  $\gamma = 0.99$ .

## 5 EXPERIMENTS

### 5.1 Training Strategy

As the shapes of input point clouds are different from each other for end-to-end learning, the batch size is set to 1 in the proposed framework. We accumulate *iteration\_size* losses and gradients to emulate the process of batch optimization. The data augmentation is injected during training with random scaling  $\in [0.8, 1.2]$  and random rotation  $\in [0^\circ, 360^\circ)$  to make sure the proposed network is robust to the variation of viewpoint.

## 5.2 Comparison with FR-PCQA Metrics

To prove the performance of the proposed NR-PCQA model, we conduct the validation experiment on the proposed large-scale dataset. The dataset with pseudo MOS established in Section 3 is divided into two parts: the training set and testing set. The training set and testing set contain the distorted samples generated from 100 reference point clouds and 4 reference point clouds respectively for no overlapping in context.

We use Pearson Linear Correlation Coefficient (PLCC) and SROCC to quantify the performance of the quality assessment methods.

PLCC measures the linear correlation between MOS and predicted quality scores via

$$PLCC(p_i, \hat{p}_i) = \frac{\sum_i (p_i - p_m)(\hat{p}_i - \hat{p}_m)}{\sqrt{\sum_i (p_i - p_m)^2} \sqrt{\sum_i (\hat{p}_i - \hat{p}_m)^2}} \quad (11)$$

where  $p_i$  is the true MOS,  $\hat{p}_i$  is the predicted quality score, and  $p_m$  and  $\hat{p}_m$  are their arithmetic mean.

SROCC assesses the monotony between MOS and predicted quality scores. It is defined as

$$SROCC(p_i, \hat{p}_i) = 1 - \frac{6 \sum_{i=1}^L (m_i - n_i)^2}{L(L^2 - 1)} \quad (12)$$

where  $L$  is the number of distorted point clouds,  $m_i$  is the rank of  $p_i$  in the MOS scores, and  $n_i$  is the rank of  $\hat{p}_i$  in the predicted quality scores. SROCC can be reformulated as

$$SROCC(p_i, \hat{p}_i) = PLCC(R(p_i), R(\hat{p}_i)) \quad (13)$$

where  $R$  denotes the ranking operation. SROCC is independent of numerical values.

We compare the performance of the proposed method with the existing FR-PCQA metrics, including p2point [14, 32], p2plane [29, 32], Hausdorff.p2point [14, 32], Hausdorff.p2plane [29, 32], PSNRyuv [32], Hausdorff.PSNRyuv [32], PCQM [31], GraphSIM [53] and MPED [52]. All the FR-PCQA results are calculated based on the source code released by authors. The results are summarized in Table 10, where the rows represent the quality assessment metrics and columns give the results of overall SROCC and PLCC.

From Table 10, we can see that the performance of the proposed NR method can be comparable to that of existing FR metrics. Specifically, the overall SROCC and PLCC of our proposed method are 0.618770 and 0.597554. The point-based metrics (such as p2point and p2plane) cannot respond to color distortion, leading to poor overall performance. The unsatisfactory performance of other metrics (such as PSNRyuv, PCQM and GraphSIM) derive from the fact that these metrics have poor performance for some compression distortions (such as V-PCC distortions). For these compression distortions, the massive increase in points after reconstruction cannot be handled well [53]. The experiment results demonstrate the effectiveness of the proposed NR-PCQA method.

## 5.3 Cross-dataset Validation

To verify the effectiveness of the generated pseudo MOS and the generalization of the proposed ResSCNN, we evaluate the performance of ResSCNN on SJTU-PCQA dataset [54] whose reference point clouds and superimposed multiple distortions have not been covered by the proposed LS-PCQA. Specifically, We train the network on our proposed LS-PCQA dataset and evaluate the performance on SJTU-PCQA dataset. The range of Cartesian coordinates for samples in SJTU-PCQA is scaled to that in LS-PCQA before evaluating. The results are listed in Table 11.

Table 10. Performance comparison of different quality assessment metrics on testing set of LS-PCQA dataset.

	mseF,PSNR (p2point)	mseF,PSNR (p2plane)	h.,PSNR (p2point)
SROCC	0.301049	0.290731	0.262240
PLCC	0.611082	0.586714	0.524797
	h.,PSNR (p2plane)	PSNRyuv	h.PSNRyuv
SROCC	0.264313	0.616367	0.571519
PLCC	0.532612	0.625247	0.595404
	PCQM	GraphSIM	MPED
SROCC	0.537464	0.459895	0.671343
PLCC	0.398444	0.427098	0.707378
	ResSCNN		
SROCC	0.618770		
PLCC	0.597554		

Table 11. Performance comparison of different quality assessment metrics on SJTU-PCQA dataset.

	mseF,PSNR (p2point)	mseF,PSNR (p2plane)	h.,PSNR (p2point)
SROCC	0.718127	0.666889	0.583088
PLCC	0.669942	0.627026	0.598841
	h.,PSNR (p2plane)	PSNRyuv	h.PSNRyuv
SROCC	0.598321	0.620676	0.458990
PLCC	0.612940	0.631057	0.478099
	PCQM	GraphSIM	MPED
SROCC	0.846495	0.841346	0.930586
PLCC	0.860261	0.857253	0.921873
	ResSCNN		
SROCC	0.557055		
PLCC	0.581143		

We can see from Table 11 that the overall SROCC and PLCC of our proposed method achieve 0.557055 and 0.581143 respectively, which can be comparable to several FR-PCQA metrics. The results on SJTU-PCQA dataset prove the robustness and generalization of our proposed ResSCNN, especially the generalization ability for unknown types of point clouds and distortions. Besides, the cross-dataset validation demonstrates that the established large-scale dataset can contribute in the training of learning-based NR-PCQA models.

#### 5.4 Analysis of Sensitivity and Robustness

We conduct two additional experiments to demonstrate the effectiveness of network depth in terms of different distortions. The first experiment uses the features from the first block (denoted as Block1) in Fig. 7 only, while another experiment uses the features from the last block (denoted as Block4) only. The use of features in different depths provides inconsistent performance for the same type of distortion. For example, the shallow features are better at dealing with some detail

distortions and visually obvious distortions such as color noise, while the deep features are better at dealing with distortions that need to be understood globally such as reconstruction distortion. The reason is that the semantic information of CNN from the shallow to deep layers has specific characteristics [12]. The shallow features provide rich details while deep features contain more conceptual information. Therefore, fusing hierarchical features would provide significant gain on improving sensitivity to various distortions.

Next, we demonstrate the robustness of the hierarchical features. We compare the performance between the single-layer features and hierarchical features, as shown in Fig. 9. It can be seen from Fig. 9 that the features from Block1 play a more important role in the quality prediction, because most of the distortion types in our newly established dataset are detail distortions and visually obvious distortions. In contrast to the performance in terms of overall SROCC, the robustness of Block1 features is worse than that of the hierarchical features. We use the mean of SROCC among all distortion types to measure the robustness. We can see from Table 12 that the average SROCC of hierarchical features, which is 0.556881, is higher than that of Block1 features, which is 0.427633. Thus, the hierarchical feature exhibits better robustness.

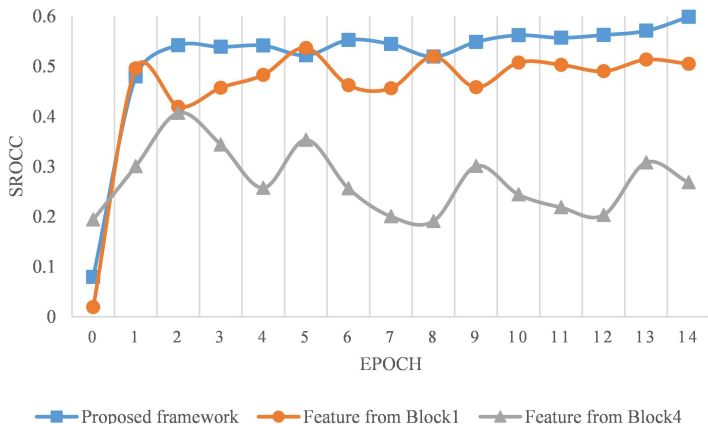


Fig. 9. SROCC results using features from different depths in the testing set.

Table 12. Average SROCC results derived from using features from Block1 only and Block4 only.

	proposed hierarchical	feature from Block1	feature from Block4
Average SROCC	0.556881	0.427633	0.341205

### 5.5 Effect of Residual Module

Instead of sequentially connecting the sparse convolutional layers, we connect the second and third layers in each block to the residual pattern. In order to elaborate the effectiveness of the residual module, we conduct a validation experiment where we compare the performance of the proposed framework in Fig. 7 and the framework with residual connection removed. The results are given in Fig. 10. We can see from Fig. 10 that the residual connection promotes the convergence of the loss function and improves the accuracy of quality prediction.

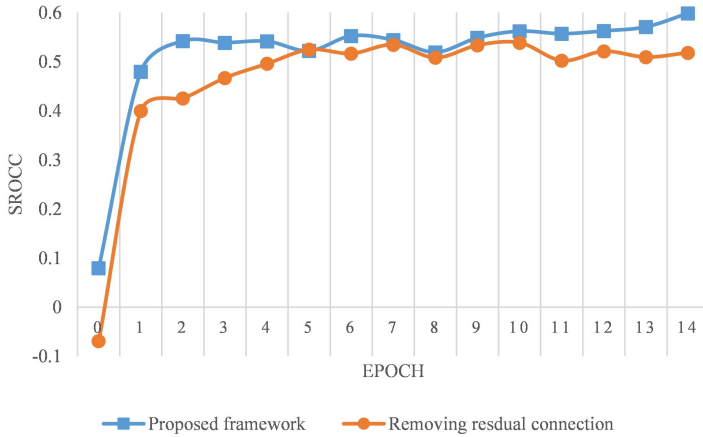


Fig. 10. SROCC result comparison of whether to use the residual connection in the testing set.

The reason is that to ensure the consistent shape of output features, increase the calculation speed and decrease the number of parameters, global pooling is carried out to reduce the dimension of output from each block. After global pooling, some part of the information in the features is partially damaged. To enhance the representativeness of output features, we compensate for the information loss using the input through the residual connection. As a result, the final design of our proposed network is the one shown in Fig. 7.

### 5.6 Comparison with Other NR-PCQA Backbones

To prove the effectiveness of the proposed ResSCNN, we compare ResSCNN with other learning-based backbones. Since no other learning-based NR-PCQA methods have been proposed at present, we design additional learning-based NR-PCQA backbones for comparison using PointNet [35].

**Modified PointNet as Backbone.** PointNet [35] is proven to be a successful feature extraction backbone which applies one-dimensional convolution to extract semantic features of geometrical attributes. We conduct experiments to evaluate the performance of PointNet in quality assessment as the backbone. Since PointNet only deals with the geometrical attributes, we design two modified PointNet as feature extraction backbones to take both the geometrical and color attributes into count. The two designed frameworks are shown in Fig. 11 (top) and Fig. 11 (bottom).

The first modified PointNet backbone (denoted as PointNet1) is shown in Fig. 11 (top). *Transform* is the transformation module used in PointNet [35] for input permutation invariance, and *MLP* stands for multi-layer perceptron which contains multiple convolutional layers. We take  $n$  points as input and apply input and feature transformations. After the  $64 \times 1$  geometrical features have been extracted, the  $3 \times 1$  color attributes are concatenated with the geometrical features to generate  $67 \times 1$  composite features. The composite features are fed into *MLP* to generate the  $1024 \times 1$  features. The final point features are aggregated by max pooling.

In the second modified PointNet backbone (denoted as PointNet2) as shown in Fig. 11 (bottom), two parallel PointNet structures are established for geometrical and color features. Considering that the transformation module in PointNet has been demonstrated to have only a weak effect in [35] and doesn't apply to the color attributes, *Transform* is removed here. The features derived from two branches are concatenated and then max pooled to generate the final  $2048 \times 1$  features.

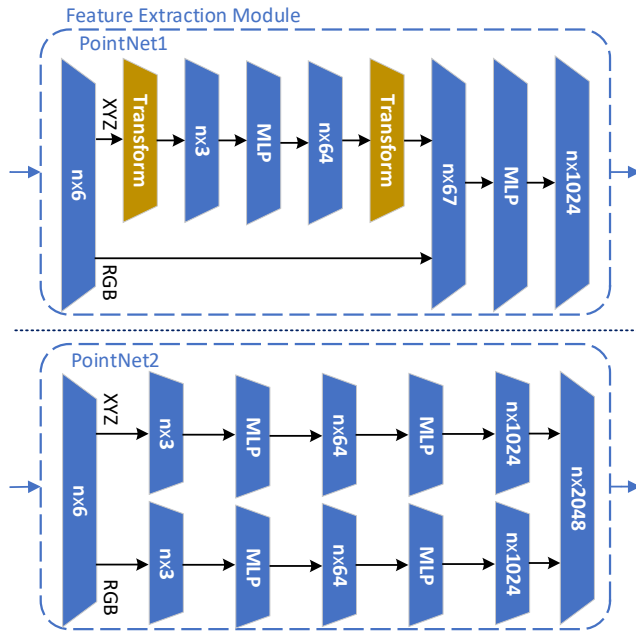


Fig. 11. Structure of modified PointNet as feature extraction backbone.

The results of modified PointNet as feature extraction backbone are shown in Fig. 12. We can see from Fig. 12 that the second framework performs better than the first one. Then we compare the results of the second modified PointNet with those of the proposed ResSCNN. We can see from Fig. 12 that the modified PointNet performs poorer than our proposed network. As a result, the features extracted from our proposed network are more appropriate for the PCQA task than those extracted from PointNet.

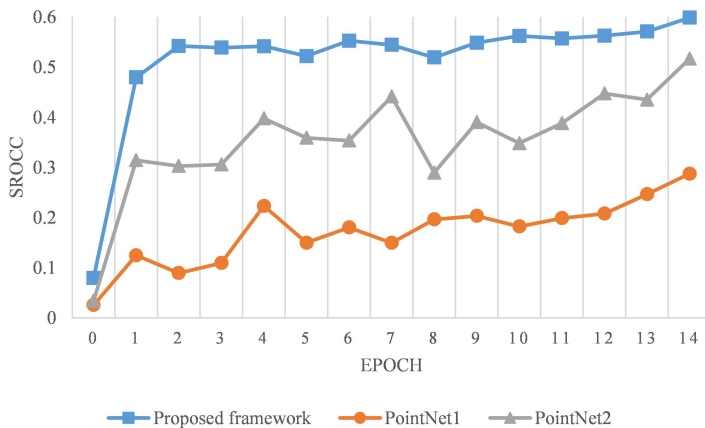


Fig. 12. Comparison between the results of modified PointNet and the results of ResSCNN in the testing set.

## 6 CONCLUSION

In this work, we investigated the learning-based NR-PCQA method and proposed the first NR-PCQA framework. To meet the requirement of data scale for learning-based metric, we firstly established a PCQA dataset of the largest size at present, which contains 24,024 distorted samples derived from 104 original reference point clouds with 33 impairment types at 7 distortion levels. Leveraging our newly established dataset, the first NR-PCQA method based on the sparse CNN was proposed. Experiment results have demonstrated the efficiency of our proposed NR-PCQA method whose performance is comparable to that of the existing FR-PCQA metrics. In addition to the proposed sparse CNN backbone, other feature extraction backbones were also evaluated. We showed that our proposed network performs better in the PCQA task.

## 7 ACKNOWLEDGEMENT

This paper is supported in part by National Key Research and Development Project of China (2018YFE0206700, 2018YFB1802201), National Natural Science Foundation of China (61971282, U20A20185), and Scientific Research Plan of the Science and Technology Commission of Shanghai Municipality (18511105402). Y. Liu and Q. Yang contributed equally to this work. Corresponding author: Y. Xu.

## REFERENCES

- [1] [n.d.]. Free3d. <https://free3d.com/3d-models>.
- [2] [n.d.]. Image and Video Quality Assessment Research at LIVE. <http://live.ece.utexas.edu/research/quality/>.
- [3] [n.d.]. JPEG Pleno Database. <http://uspaulopc.di.ubi.pt/>.
- [4] [n.d.]. MPEG Inanimate DataSets. [http://mpegfs.int-evry.fr/MPEG/PCC/DataSets/pointCloud/CfP/datasets/Static\\_Objects\\_and\\_Scenes/Inanimate\\_Objects/](http://mpegfs.int-evry.fr/MPEG/PCC/DataSets/pointCloud/CfP/datasets/Static_Objects_and_Scenes/Inanimate_Objects/).
- [5] [n.d.]. MPEG People DataSets. [http://mpegfs.int-evry.fr/MPEG/PCC/DataSets/pointCloud/CfP/decoded/Dynamic\\_Objects/People/8i/](http://mpegfs.int-evry.fr/MPEG/PCC/DataSets/pointCloud/CfP/decoded/Dynamic_Objects/People/8i/).
- [6] [n.d.]. MPEG Static Object and Scenes DataSets. [http://mpegfs.int-evry.fr/MPEG/PCC/DataSets/pointCloud/CfP/datasets/Static\\_Objects\\_and\\_Scenes/ULB\\_Unicorn/](http://mpegfs.int-evry.fr/MPEG/PCC/DataSets/pointCloud/CfP/datasets/Static_Objects_and_Scenes/ULB_Unicorn/).
- [7] [n.d.]. Sketchfab. <https://sketchfab.com>.
- [8] 2012. Methodology for the Subjective Assessment of the Quality of Television Pictures. Recommendation BT.500-13.
- [9] Evangelos Alexiou and Touradj Ebrahimi. 2018. Point cloud quality assessment metric based on angular similarity. In *Int. Conf. Multimedia and Expo (ICME'18)*. IEEE, 1–6.
- [10] Evangelos Alexiou and Touradj Ebrahimi. 2020. Towards a Point Cloud Structural Similarity Metric. *Int. Conf. Multimedia and Expo Workshops (ICMEW'20)* (2020), 1–3.
- [11] Evangelos Alexiou, Nanyang Yang, and Touradj Ebrahimi. 2020. PointXR: A Toolbox for Visualization and Subjective Evaluation of Point Clouds in Virtual Reality. In *2020 Twelfth International Conference on Quality of Multimedia Experience (QoMEX)*.
- [12] S. Bai, Z. He, Y. Dong, and H. Bai. 2020. Multi-Hierarchical Independent Correlation Filters For Visual Tracking. In *2020 IEEE International Conference on Multimedia and Expo (ICME)*. 1–6. <https://doi.org/10.1109/ICME46284.2020.9102759>
- [13] Christopher Choy, JunYoung Gwak, and Silvio Savarese. 2019. 4D spatio-temporal convnets: Minkowski convolutional neural networks. In *CVPR*.
- [14] Paolo Cignoni, Claudio Rocchini, and Roberto Scopigno. 1998. Metro: measuring error on simplified surfaces. In *Computer Graphics Forum*, Vol. 17. Wiley Online Library, 167–174.
- [15] Girum G. Demisse, Djamilia Aouada, and Björn Ottersten. 2018. Deformation-Based 3D Facial Expression Representation. *ACM Trans. Multimedia Comput. Commun. Appl.* 14, 1s (2018). <https://doi.org/10.1145/3176649>
- [16] Haowen Deng, Tolga Birdal, and Slobodan Ilic. 2018. PPF-FoldNet: Unsupervised Learning of Rotation Invariant 3D Local Descriptors. In *European Conference on Computer Vision*.
- [17] Haowen Deng, Tolga Birdal, and Slobodan Ilic. 2018. PPFNet: Global Context Aware Local Features for Robust 3D Point Matching. In *CVPR*.
- [18] Fei Gao and Jun Yu. 2016. Biologically inspired image quality assessment. *Signal Processing* 124, Jul. (2016), 210–219.
- [19] Benjamin Graham, Martin Engelcke, and Laurens van der Maaten. 2018. 3D semantic segmentation with submanifold sparse convolutional networks. In *CVPR*.

- [20] Benjamin Graham and Laurens van der Maaten. 2017. Submanifold Sparse Convolutional Networks. *arXiv preprint arXiv:1706.01307* (2017).
- [21] Yulan Guo, Bennamoun Mohammed, Sohel Ferdous, Min Lu, Jianwei Wan, and Kwok Ngai Ming. 2016. A comprehensive performance evaluation of 3d local feature descriptors. In *IJCV*, Vol. 116.
- [22] ITU-T, P. 2012. 1401: Methods, metrics and procedures for statistical evaluation, qualification and comparison of objective quality prediction models. *ITU-T Recommendation* (2012), 1401.
- [23] Alireza Javaheri, Catarina Brites, Fernando Pereira, and Joao Ascenso. 2019. Point Cloud Rendering after Coding: Impacts on Subjective and Objective Quality. *arXiv preprint arXiv:1912.09137* (2019).
- [24] Alireza Javaheri, Catarina Brites, Fernando Pereira, and Joao Ascenso. 2020. A generalized Hausdorff distance based quality metric for point cloud geometry. *arXiv preprint arXiv:2003.13669* (2020).
- [25] A. E. Johnson and M. Hebert. 1999. Using spin images for efficient object recognition in cluttered 3d scenes. 21, 5 (1999).
- [26] Marc Khoury, Qian-Yi Zhou, and Vladlen Koltun. 2017. Learning Compact Geometric Features. In *ICCV*.
- [27] Yutao Liu, Ke Gu, Xiu Li, and Yongbing Zhang. 2020. Blind Image Quality Assessment by Natural Scene Statistics and Perceptual Characteristics. *ACM Trans. Multimedia Comput. Commun. Appl.* 16, 3 (2020). <https://doi.org/10.1145/3414837>
- [28] Kede Ma, Zhengfang Duanmu, Qingbo Wu, Zhou Wang, and Lei Zhang. 2017. Waterloo Exploration Database: New Challenges for Image Quality Assessment Models. *IEEE Transactions on Image Processing* 26, 99 (2017), 1004–1016.
- [29] R. Mekuria, Z. Li, C. Tulvan, and P. Chou. 2016. Evaluation criteria for point cloud compression. *ISO/IEC MPEG w16332, Geneva, Switzerland* (Feb, 2016).
- [30] Gabriel Meynet, Julie Digne, and Guillaume Lavoue. 2019. PC-MSDM: A quality metric for 3D point clouds. *2019 Eleventh Int. Conf. Quality of Multimedia Experience (QoMEX'19)* (2019), 1–3.
- [31] Gabriel Meynet, Yana Nehme, and Guillaume Lavoue. 2020. PCQM: A Full-Reference Quality Metric for Colored 3D Point Clouds. *2020 Twelfth Int. Conf. Quality of Multimedia Experience (QoMEX'20)* (2020).
- [32] MRS [n.d.]. *MPEG Reference Software*. <http://mpegx.int-evry.fr/software/MPEG/PCC/TM/mpeg-pcc-dmetric>
- [33] Anass Nouri, Christophe Charrier, and Olivier Lézoray. 2017. Greyc 3D colored mesh database. *[Technical Report] Normandie Université* (2017).
- [34] Nikolay Ponomarenko, Oleg Ieremeiev, Vladimir Lukin, Karen Egiazarian, Lina Jin, Jaakko Astola, Benoit Vozel, Kacem Chehdi, Marco Carli, Federica Battisti, and C.-C. Jay Kuo. 2015. Image database TID2013: Peculiarities, results and perspectives. *Signal Processing Image Communication* 30 (2015), 57–77.
- [35] Charles R. Qi, Hao Su, Kaichun Mo, and Leonidas J. Guibas. 2017. PointNet: Deep Learning on Point Sets for 3D Classification and Segmentation. In *Proceedings of the IEEE Conference on Computer Vision and Pattern Recognition (CVPR)*.
- [36] Radu Bogdan Rusu, Nico Blodow, and Michael Beetz. 2009. Fast point feature histograms (FPFH) for 3D registration. In *ICRA*.
- [37] Radu Bogdan Rusu, Nico Blodow, Zoltan Csaba Marton, and Michael Beetz. 2008. Aligning point cloud views using persistent feature histograms. In *IROS*.
- [38] Samuele Salti, Federico Tombari, and Luigi Di Stefano. 2014. SHOT: Unique signatures of histograms for surface and texture description. 125 (2014).
- [39] Hamid R. Sheikh and Alan C. Bovik. 2006. Image information and visual quality. *IEEE transactions on image processing a publication of the IEEE signal processing society* 15, 2 (2006), 430–444.
- [40] H. R. Sheikh and A. C. Bovik. 2006. Image information and visual quality. *IEEE Transactions on image processing* 15, 2 (2006), 430.
- [41] Jia Sun, Di Huang, Yunhong Wang, and Liming Chen. 2019. Expression Robust 3D Facial Landmarking via Progressive Coarse-to-Fine Tuning. *ACM Trans. Multimedia Comput. Commun. Appl.* 15, 1 (2019). <https://doi.org/10.1145/3282833>
- [42] D. Tian, H. Ochimizu, C. Feng, R. Cohen, and A. Vetro. 2017. Evaluation metrics for point cloud compression. *ISO/IEC JTC m74008, Geneva, Switzerland* (Jan, 2017).
- [43] Federico Tombari, Samuele Salti, and Luigi Di Stefano. 2010. Unique shape context for 3d data description. In *ACM Workshop on 3D Object Retrieval*.
- [44] Eric M Torlig, Evangelos Alexiou, Tiago A Fonseca, Ricardo L de Queiroz, and Touradj Ebrahimi. 2018. A novel methodology for quality assessment of voxelized point clouds. 10752 (2018), 1075201.
- [45] Video Quality Experts Group. 2000. Final report from the video quality experts group on the validation of objective models of video quality assessment. *VQEG meeting* (2000).
- [46] Video Quality Experts Group. 2010. Report on the validation of video quality models for high definition video content. *VQEG meeting* (2010).
- [47] Irene Viola, Shishir Subramanyam, and Pablo Cesar. 2020. A color-based objective quality metric for point cloud contents. *2020 Twelfth Int. Conf. Quality of Multimedia Experience (QoMEX'20)* (2020).

- [48] Zhou Wang, Alan C Bovik, Hamid R Sheikh, and Eero P Simoncelli. 2004. Image quality assessment: from error visibility to structural similarity. *IEEE trans. Image Processing* 13, 4 (2004), 600–612.
- [49] Zhou Wang, Alan Conrad Bovik, Hamid Rahim Sheikh, and Eero P. Simoncelli. 2006. Image quality assessment: from error visibility to structural similarity. *IEEE transactions on image processing* 13, 4 (2006), 600–612.
- [50] Jinjian Wu, Jupou Ma, Fuhu Liang, Weisheng Dong, and Weisi Lin. 2020. End-to-End Blind Image Quality Prediction With Cascaded Deep Neural Network. *IEEE Transactions on Image Processing* PP, 99 (2020), 1–1.
- [51] Wufeng Xue, Lei Zhang, Xuanqin Mou, and Alan Bovik. 2014. Gradient Magnitude Similarity Deviation: A Highly Efficient Perceptual Image Quality Index. *IEEE Transactions on Image Processing* 23, 2 (2014), 684–695.
- [52] Qi Yang, Siheng Chen, Yiling Xu, Jun Sun, M. Salman Asif, and Zhan Ma. 2021. Point Cloud Distortion Quantification based on Potential Energy for Human and Machine Perception. *arXiv preprint arXiv:2103.02850* (2021).
- [53] Qi Yang, Zhan Ma, Yiling Xu, Zhu Li, and Jun Sun. 2020. Inferring point cloud quality via graph similarity. *arXiv preprint arXiv:2006.00497* (2020).
- [54] Q. Yang, Z. Ma, Y. Xu, R. Tang, and J. Sun. 2020. Predicting the Perceptual Quality of Point Cloud: A 3D-to-2D Projection-Based Exploration. *IEEE Transactions on Multimedia* (2020).
- [55] Zijian Yew and GimHee Lee. 2018. 3DFeat-Net: Weakly Supervised Local 3D Features for Point Cloud Registration. In *European Conference on Computer Vision*.
- [56] Andy Zeng, Shuran Song, Matthias Niener, Matthew Fisher, and Jianxiong Xiao. 2017. 3Dmatch: Learning the matching of local 3D geometry in range scans. In *CVPR*.

## A ALL THE REFERENCE POINT CLOUDS

In this work, 104 different point cloud content, including 28 human body models, 48 animal body models and 28 inanimate objects, are chosen as the original point cloud samples. Fig. 13 illustrates the snapshots of all the reference point clouds for the proposed dataset in this work.

## B DETAILS FOR DISTORTION TYPES IN LS-PCQA DATASET

The details for each distortion type in the established dataset are given in the following.

- (1) Additive Gaussian noise: The photometric attributes are added with Gaussian noise with different intensities. The signal to noise ratios of different distortion levels are respectively 13dB, 11dB, 9dB, 7dB, 5dB, 3dB, and 1dB.
- (2) Color noise: Color noise is applied to the photometric attributes of the points. We inject the noise for 10%, 20%, 30%, 40%, 50%, 60%, and 70% points that are randomly selected, where noise levels are respectively and again randomly given within  $\pm 10, \pm 20, \pm 30, \pm 40, \pm 50, \pm 60,$  and  $\pm 70$  for corresponding points (e.g., 10% random points with  $\pm 10$  noise, 30% random points with  $\pm 30$ , and so on so forth). Noise is equally applied to R, G, B attributes. Cropping is used if the noisy intensity  $\tilde{p} = p + n$ , is out of the range of  $[0, 255]$ , i.e., if  $\tilde{p} < 0$ ,  $\tilde{p} = 0$ ; and if  $\tilde{p} > 255$ ,  $\tilde{p} = 255$ .
- (3) High-frequency noise: Gaussian noise is added to the high-frequency part of the photometric attributes of point clouds. The cutoff frequency of the high-pass filter is set to 40,000 Hz. The variances of the added Gaussian noise are 0.001, 0.003, 0.005, 0.0075, 0.01, 0.03, and 0.05 respectively.
- (4) Quantization noise: The quantization noise is due to color quantization. To implement the quantization noise, we equally quantify the photometric attributes. For different distortion levels, we set the quantization step to 27, 33, 39, 47, 55, 65, and 76 respectively.
- (5) Mean shift (intensity shift): The mean shift is applied to the photometric attributes of the point clouds. The photometric attributes are respectively enhanced 10, 20, 30, 40, 50, 60, and 70.
- (6) Contrast change: The contrast change is to contaminate the photometric attributes of point clouds in perceptual contrast. To implement the contrast change, the R, G, B attributes are 1.1, 1.2, 1.3, 1.4, 1.5, 1.6, and 1.7 power of original values respectively.



- (7) Change of color saturation: The color saturation distortion is to contaminate the photometric attributes of point clouds in color saturation. The saturation of photometric attributes is computed based on lightness. Then the increment of saturation is set to  $-25\%$ ,  $-50\%$ ,  $-75\%$ ,  $-100\%$ ,  $-125\%$ ,  $-150\%$ , and  $-200\%$  respectively.
- (8) Spatially correlated noise: The photometric attributes of point clouds are added to the correlated Gaussian noise whose standard deviation is 10, 20, 30, 40, 50, 60, and 70 respectively.
- (9) Multiplicative Gaussian noise: To implement the multiplicative Gaussian noise, the photometric attributes of point clouds are multiplied by the Gaussian noise with different intensities. The intensities of multiplied Gaussian noise are set to 10, 30, 55, 80, 105, 130, and 155 dBm.
- (10) Color quantization with dither: This distortion is produced by the `rgb2ind` operation. To implement the color quantization with dither distortion, we convert the true color R, G, B to index color. The index number of colors for different distortion levels is separately set to 24, 16, 12, 8, 6, 4, and 2.
- (11) Octree Compression: This distortion comes from the octree pruning method. Octree pruning removes leaf nodes to adjust tree resolution for compression. Here, we have experimented different compression levels by removing points at 8%, 10%, 12%, 14%, 16%, 18% and 20%.
- (12) Down-sampling: The down-sampling distortion is caused by the missing points. We randomly down-sample the point clouds by removing 15%, 30%, 45%, 60%, 70%, 80%, 90% points from the original point clouds.
- (13) Salt-pepper noise: The salt-and-pepper noise is the white or black spots that appear randomly in the photometric attributes of point clouds. To produce the salt-and-pepper noise for different distortion levels, we set the proportion of random points where the salt-and-pepper noise emerges to 0.02, 0.05, 0.1, 0.15, 0.2, 0.25, and 0.30 respectively.
- (14) Rayleigh noise: The Rayleigh noise is equally added to all the photometric attributes. We use the function `raylrnd()` in Matlab to generate the Rayleigh noise. For different distortion levels, parameter  $B$  of `raylrnd()` is set to 10, 20, 30, 40, 50, 60, and 70 separately.
- (15) Gamma noise: Gamma noise obeys the Gamma curve distribution. To realize the Gamma noise,  $B$  noises which obey exponential distribution are superimposed, formulated as

$$E = \sum_{i=1}^B E_i = \sum_{i=1}^B -\frac{1}{a} \ln[1 - U(0, 1)]$$

In this work,  $B$  is set to 3 and for different distortion levels,  $a$  is set to 0.1, 0.08, 0.07, 0.06, 0.05, 0.04, and 0.03 respectively.

- (16) Uniform noise (white noise): The white noise is added to the photometric attributes of point clouds. To implement this distortion, we randomly offset R, G, B values of each point among  $[-10,10]$ ,  $[-20,20]$ ,  $[-30,30]$ ,  $[-40,40]$ ,  $[-50,50]$ ,  $[-60,60]$ , and  $[-70,70]$  respectively.
- (17) Poisson noise: The Poisson noise is equally added to all the photometric attributes. We use the function `poissrnd()` in Matlab to generate the Poisson noise. For different distortion levels, parameter  $B$  of `poissrnd()` is set to 10, 20, 30, 40, 50, 60, and 70 separately.
- (18) Gaussian geometry shifting: We apply Gaussian distributed geometric shift to each point randomly. In this study, all the points will be augmented with a Gaussian geometry shift whose standard deviation is 0.1%, 0.25%, 0.4%, 0.55%, 0.7%, 0.85%, 1% of the bounding box respectively.
- (19) Uniform geometry shifting: Uniform geometry shifting is applied to the geometry attributes of point clouds. The shifting are applied in 10%, 20%, 30%, 40%, 50%, 60%, and 70% points that are randomly selected, where the shifting ranges are respectively  $\pm 0.5\%$ ,  $\pm 1\%$ ,  $\pm 2\%$ ,  $\pm 3\%$ ,

- $\pm 4\%$ ,  $\pm 5\%$ , and  $\pm 7\%$  for corresponding points (e.g., 10% random points with  $\pm 0.5\%$  noise, 30% random points with  $\pm 2\%$ , and so on so forth). Noise is equally applied to x, y, z locations.
- (20) Local loss: To implement this distortion, we define the space anchor with the size of  $0.3^*[dx, dy, dz]$ . With the increase of distortion level, the additional 1, 1, 2, 2, 3, 3, 4 anchors are select for each distortion level on the basis of the selected anchors in the previous distortion level (e.g., after 1 + 1 space anchors are selected for distortion of level 2, another 2 different anchors are selected for distortion of level 3). Then the points in the selected anchors are removed.
  - (21) Local offset: The selection of anchors is as same as that in the local loss distortion. The difference is that for each distortion level, the values of geometry attributes of each point in the selected anchors will increase by 100.
  - (22) Local rotation: The selection of anchors is as same as that in the local loss distortion. The difference is that for each distortion level, the points in the selected anchors will be rotated 20, 25, 30, 35, 40, 45, and 50 degrees respectively along the x-axis.
  - (23) Luminance distortion: Luminance distortion is to contaminate the point clouds in the luminance component. To implement the luminance distortion, the photometric attributes of point clouds are converted from RGB space to YCbCr space. Then the luminance component is added to an offset which is 20, 50, 70, 90, 110, 130, and 150 separately.
  - (24) Poisson Reconstruction: The reconstruction distortion comes from the impairment between the original and constructed point clouds. To implement this distortion, we conduct the Poisson surface reconstruction to convert the down-sampled point cloud to mesh. Then the face of mesh is randomly sampled to restore the number of points before down-sampling. The proportion of down-sampling is as same as that in the down-sampling distortion.
  - (25) GPCC with lossless geometry and lossy attributes: This distortion derives from the GPCC compression with lossless geometry and lossy attributes. To implement this distortion, we set the parameter *qp* to 27, 31, 35, 39, 43, 47, and 51 respectively and other settings follow the official instance of lossless-geometry-lossy-attributes using the *mpeg - pcc - tmc13* toolkit.
  - (26) GPCC with lossless geometry and nearlossless attributes: This distortion derives from the GPCC compression with lossless geometry and nearlossless attributes. To implement this distortion, we set the parameter *qp* to 10, 16, 22, 28, 34, 40, and 46 respectively and other settings follow the official instance of lossless-geometry-nearlossless-attributes.
  - (27) GPCC with lossy geometry and lossy attributes: This distortion derives from the GPCC compression with lossy geometry and lossy attributes. To implement this distortion, we set the parameter *positionQuantizationScale* to 0.9375, 0.875, 0.75, 0.5, 0.25, 0.125, 0.0625 and set *qp* to 27, 31, 35, 39, 43, 47, 51 respectively. Other settings follow the official instance of lossy-geometry-lossy-attributes.
  - (28) VPCC with lossless geometry and lossy attributes: This distortion derives from the VPCC compression with lossless-geometry-lossy-attributes. To implement this distortion, we set the parameter *textureQP* to 22, 27, 32, 37, 42, 47, 51 respectively and set *occupancyPrecision* to 2, 4, 4, 4, 4, 4, 4 respectively. Other settings follow the official instance of lossless-geometry-lossy-attributes using the *mpeg - pcc - tmc2* toolkit.
  - (29) VPCC with lossy geometry and lossless attributes: This distortion derives from the VPCC compression with lossy-geometry-lossless-attributes. To implement this distortion, we set the parameter *geometryQP* to 22, 27, 32, 37, 42, 47, 51 respectively and set *occupancyPrecision* to 2, 4, 4, 4, 4, 4, 4 respectively. Other settings follow the official instance of lossy-geometry-lossless-attributes.
  - (30) VPCC with lossy geometry and lossy attributes: This distortion derives from the VPCC compression with lossy geometry and lossy attributes. To implement this distortion, we set the parameter *geometryQP* to 16, 20, 24, 28, 32, 36, 40 and set *textureQP* to 22, 27, 32, 37,

42, 47, 51 respectively. The *occupancyPrecision* is set to 2, 4, 4, 4, 4, 4 respectively. Other settings follow the official instance of lossy-geometry-lossy-attributes.

- (31) AVS with limitlossy geometry and lossy attributes: This distortion derives from the AVS compression with limitlossy-geometry-lossy-attributes. To implement this distortion, we set the parameter *geom\_quant\_step* to 1.14286, 1.33333, 2, 4, 8, 12, 16 respectively and set *attr\_quant\_param* to 8, 16, 24, 32, 40, 44, 48 respectively. Other settings follow the official instance of limitlossy-geometry-lossy-attributes using the *avs - pcc - pcm2* toolkit.
- (32) AVS with lossless geometry and limitlossy attributes: This distortion derives from the AVS compression with lossless-geometry-limitlossy-attributes. To implement this distortion, we set the parameter *attr\_quant\_param* to 8, 16, 24, 32, 40, 44, 48 respectively and other settings follow the official instance of lossless-geometry-limitlossy-attributes.
- (33) AVS with lossless geometry and lossy attributes: This distortion derives from the AVS compression with lossless-geometry-lossy-attributes. To implement this distortion, we set the parameter *attr\_quant\_param* to 8, 16, 24, 32, 40, 44, 48 respectively and other settings follow the official instance of lossless-geometry-lossy-attributes.